UC Santa Cruz

UC Santa Cruz Previously Published Works

Title

Multifaceted Changes in Synaptic Composition and Astrocytic Involvement in a Mouse Model of Fragile X Syndrome

Permalink

https://escholarship.org/uc/item/79v7g3g9

Journal

Scientific Reports, 9(1)

ISSN

2045-2322

Authors

Simhal, Anish K
Zuo, Yi
Perez, Marc M
et al.

Publication Date

2019

DOI

10.1038/s41598-019-50240-x

Peer reviewed

SCIENTIFIC REPORTS
natureresearch

OPEN

Multifaceted Changes in Synaptic Composition and Astrocytic Involvement in a Mouse Model of Fragile X Syndrome

Anish K. Simhal [1], Yi Zuo [2], Marc M. Perez[3], Daniel V. Madison[3], Guillermo Sapiro[1,4] & Kristina D. Micheva[3]

Fragile X Syndrome (FXS), a common inheritable form of intellectual disability, is known to alter neocortical circuits. However, its impact on the diverse synapse types comprising these circuits, or on the involvement of astrocytes, is not well known. We used immunofluorescent array tomography to quantify different synaptic populations and their association with astrocytes in layers 1 through 4 of the adult somatosensory cortex of a FXS mouse model, the FMR1 knockout mouse. The collected multi-channel data contained approximately 1.6 million synapses which were analyzed using a probabilistic synapse detector. Our study reveals complex, synapse-type and layer specific changes in the neocortical circuitry of FMR1 knockout mice. We report an increase of small glutamatergic VGluT1 synapses in layer 4 accompanied by a decrease in large VGluT1 synapses in layers 1 and 4. VGluT2 synapses show a rather consistent decrease in density in layers 1 and 2/3. In all layers, we observe the loss of large inhibitory synapses. Lastly, astrocytic association of excitatory synapses decreases. The ability to dissect the circuit deficits by synapse type and astrocytic involvement will be crucial for understanding how these changes affect circuit function, and ultimately defining targets for therapeutic intervention.

Fragile X Syndrome (FXS) is the most common inheritable form of intellectual disability, affecting approximately 1 in 7,000 males and 1 in 11,000 females across all races and ethnic groups[1]. FXS patients display a wide spectrum of phenotypes, including moderate to severe intellectual disability, autistic behavior, macroorchidism, predisposition to epileptic seizures, and facial abnormalities[2–4]. FXS is caused by the silencing of the FMR1 gene, which encodes the Fragile X Mental Retardation Protein (FMRP). FMRP is known to play an important role in translation, trafficking, and targeting of a large number of mRNAs in neurons[5–7]. FMRP also binds to many proteins, suggesting its involvement in a wide variety of functions, such as genome stability regulation, cell differentiation, and ion channel gating[8]. Because FMRP participates in a multitude of processes in cells, it has proven difficult to understand how FMRP deficiency affects the synapses and neuronal circuits in brain to cause the FXS pathology.

The mouse model of this disease, the FMR1 knockout mice, display similar phenotypes to human FXS, such as deficiency in learning and memory[9–11], sensory processing[12,13], and social behaviors[14,15]. However, despite these profound neurological and behavioral deficits, the reported changes at synapses have been rather subtle, with basic synaptic neurotransmission seemingly unaffected. At the synaptic functional level, FMR1 KO mice display region-specific deficits in plasticity, such as abnormal long-term potentiation (LTP) and long-term depression (LTD)[8]. Many of the molecular signaling pathways at synapses appear dysregulated, but the changes are often region and neuron-type specific, and the contributions of specific signaling pathways to the Fragile X pathology have been difficult to untangle[16]. At the synaptic structural level, the most obvious difference is the higher density of immature, long and thin dendritic spines of pyramidal neurons in the cortex of adult FMR1 KO mice compared to WT controls[11–15].

[1]Department of Electrical Engineering, Duke University, Durham, USA. [2]Department of Molecular, Cell and Developmental Biology, University of California, Santa Cruz, USA. [3]Department of Molecular and Cellular Physiology, Stanford University School of Medicine, Stanford, USA. [4]Departments of Biomedical Engineering, Computer Sciences, and Math, Duke University, Durham, USA. Correspondence and requests for materials should be addressed to A.K.S. (email: aksimhal@gmail.com)

The unusually long and thin spines which are also found in fixed tissues of FXS patients[9,10,17,18], are similar to the immature spines observed during development[19–21]. This observation has led to a popular hypothesis that the absence of FMRP in the nervous system causes a defect in spine maturation and pruning, which in turn alters synaptic connectivity and ultimately results in behavioral defects[6,7,22–24]. While dendritic spine morphology and structural dynamics are good indicators of modifications in synaptic connectivity[25–27], they cannot fully represent the diversity of cortical synapses. For example, the majority of inhibitory synapses terminate on dendritic shafts and somata, and are thus not accounted for by changes at spines. Among the excitatory synapses terminating on spines there are cortico-cortical synapses containing the vesicular glutamate transporter VGluT1 and thalamo-cortical synapses containing VGluT2[28,29], which have very different functions in the cortical circuitry. The impact of FXS is likely to be dependent on synapse type because of the differential expression of FMRP across neuronal types[30]. Indeed, a recent study using highly multiplexed array tomography showed the varied impact of FXS on synaptic populations of cortical layer 4 and 5 in FMR1 KO mice[31].

To add a further layer of complexity, FXS may also affect certain non-neuronal cells. As the most abundant glial cells in the mammalian brain, astrocytes modulate synaptic structure and function[32] and are implicated in many neurodevelopmental diseases[33]. In the mouse brain, astrocytes also express FMRP[34], and FMR1 KO mice have fewer hippocampal synapses associated with astrocytes[35]. Interestingly, astrocyte-specific deletion of FMR1 leads to significantly more immature spines in the mouse motor cortex due to overproduction of spines during development[36]. Whether such astrocytic contribution varies according to synapse type is not yet known.

To better understand the synapse type-specific effects of FXS on the neocortical synaptic circuitry, we investigated the changes in different synaptic populations and their association with astrocytes in the adult mouse somatosensory cortex, an area in which a variety of deficits have been reported for FMR1 KO mice[37–39]. We focused on the superficial cortical layers where live-imaging studies have revealed changes in dendritic spine formation and turnover[37,40], but the synapse type specificity of the FXS effects is unknown. In order to investigate large numbers of synapses of different types, we used immunofluorescent array tomography (IF-AT) which allows for the light level detection of individual synapses within brain tissue, and the ability to apply multiple markers to distinguish synapse types[41,42]. Synaptic density was quantified using automatic synapse detection methods previously developed by our group[43,44]. Our results reveal multifaceted changes in the composition and astrocytic involvement in the synaptic circuitry of the somatosensory cortex of adult FMR1 KO mice.

Methods

Overview. The methods section is divided into two main components — data generation and computational analysis. The data generation section specifies the types of mice used, the antibodies used, and the imaging methodology. The computational analysis section highlights the methods used to automatically analyze the array tomography data, including the detection of synapses by their specific type and the detection of astrocytes. Processing and imaging each mouse took ten days on average, resulting in approximately 40GB of image data. The analysis scripts, running in parallel, took eleven days on a twelve core computer and generated approximately 800GB of auxiliary data.

Data generation. The datasets investigated were obtained from the somatosensory cortex of adult mice and represent layers one through four. The somatosensory cortex was chosen because of the well-documented deficits in FMR1 KO mice in this cortical region[37–39]. We focused on the superficial cortical layers for which more information is available through live imaging studies[37,40]. The average dataset volume was 135,588 μm^3.

Animals. Mice were group-housed in the University of California, Santa Cruz (UCSC) animal facility, with 12 hour light-dark cycles and access to food and water *ad libitum*. All procedures were performed in accordance with protocols approved by the Animal Care and Use Committee (IACUC) of UCSC. FMR1 KO mice were obtained from Dr. Stephen T. Warren, Emory University. Thy1-YFP-H mice were purchased from JAX. All mice were backcrossed with C57BL/6 mice more than 10 generations to produce congenic strains. For the current experiments, YFP+ WT males were crossed with YFP- FMR1+/− females, and only male offspring litter-mates were used for the experiments. WT mice refer to FMR1+/y, and KO mice are FMR1−/y. Because the YFP expression was highly variable between animals, we did not use it in the analysis. Four KO mice and three WT mice were used for the analysis. The mice were four months old when they were sacrificed. Further details about the mice are in Supplemental Table S1.

Array tomography. The tissue was prepared using standard array tomography protocols[42]. The mice were anesthetized by halothane inhalation and their brains quickly removed, cut into 2 *mm* slices, fixed by immersion in 4% paraformaldehyde in phosphate-buffered saline (PBS) for 1 hour at room temperature, then left in the fixative overnight at 4 °C. After rinsing in PBS, the somatosensory cortex was dissected out, quenched in 50 *mM* glycine in PBS for 30 minutes and dehydrated in a series of ethanol washes (50%, 70%, 70%) at 4 °C, then infiltrated and embedded in LRWhite resin in gelatin capsules, and polymerized at 50 °C for 24 hours.

To prepare ribbons of serial sections, the blocks were trimmed around the tissue to the shape of a trapezoid, and glue (Weldwood Contact Cement diluted with xylene) was applied with a thin paint brush to the leading and trailing edges of the block pyramid. The embedded plastic block was cut on an ultramicrotome (Leica Ultracut EM UC6) into 70 *nm*-thick serial sections, which were mounted on gelatin-coated coverslips.

Immunolabeling. Sections were processed for standard indirect immunofluorescence, as described in[42]. Antibodies were obtained from commercial sources and are listed in Table 1. Array tomography specific controls are presented in Supplemental Table S2. The sections were incubated in 50 mM glycine in TBS for 5 minutes, followed by blocking solution (0.05% Tween-20 and 0.1% BSA in TBS) for 5 minutes. The primary antibodies were diluted in blocking solution as specified in Table 1, and were applied for 2 hours at room temperature or overnight

Antigen	Host	Antibody Source	RRID	Dilution
Synapsin	Rabbit	Cell Signaling 5297	RRID:AB_2616578	1:100
PSD95	Rabbit	Cell Signaling 3450	RRID:AB_2292883	1:100
VGluT1	Guinea pig	Millipore AB5905	RRID:AB_2301751	1:5000
VGluT2	Guinea pig	Millipore AB2251	RRID:AB_2665454	1:5000
GAD2	Rabbit	Cell Signaling 5843	RRID:AB_10835855	1:100
Gephyrin	Mouse	NeuroMab 75-443	RRID:AB_2636851	1:100
Glutamine synthetase	Mouse	BD Biosciences 610517	RRID:AB_397879	1:25

Table 1. Antibodies used for the experiments.

at 4 °C. After a 15 minutes wash in TBS, the sections were incubated with Alexa dye-conjugated secondary antibodies, highly cross-adsorbed (Life Technologies), diluted 1:150 in blocking solution for 30 minutes at room temperature. Finally, sections were washed with TBS for 15 minutes, rinsed with distilled water and mounted on glass slides using SlowFade Gold Antifade Mountant with DAPI (Invitrogen). After the sections were imaged, the antibodies were eluted using a solution of 0.2 M NaOH and 0.02% SDS for 20 minutes, and new antibodies were reapplied. Several rounds of elution and re-staining were applied to create a high-dimensional immunofluorescent image. Samples were immunostained side by side in pairs, consisting of one WT and one KO sample, and imaged immediately after completion of staining.

Imaging method. The immunostained ribbons of sections were imaged on an automated epifluorescence microscope (Zeiss AxioImager Z1) using a 63x Plan-Apochromat 1.4 NA oil objective. For each section from the ribbon, an area of 140 $\mu m \times$ 400 μm was imaged and this area encompassed layers 1 through 4. The entire imaged volume was analyzed, but it was subdivided into separate subvolumes corresponding to the different layers. To define the position list for the automated imaging, a custom Python-based graphical user interface, MosaicPlanner (obtained from https://code.google.com/archive/p/smithlabsoftware/), was used to automatically find corresponding locations across the serial sections. Images from different imaging sessions were registered using a DAPI stain present in the mounting medium. The images from the serial sections were also aligned using the DAPI signal. Both image registration and alignment were performed with the MultiStackReg plugin in FIJI[45].

Computational analysis. A main goal of this analysis is to examine the effects of the lack of FMRP protein on the synaptic composition of the somatosensory cortex. This requires the ability to quantify synapses by their molecular composition and their adjacency to an astrocytic process. To achieve this, we took existing methods and expanded their scope to meet the computational challenges posed by these experiments, including developing a method for detecting astrocyte processes adjacent to synapses. The computational analysis was conducted blindly. The samples were imaged in pairs of one WT and one KO mouse by MMP and the de-identified image files were sent to AKS for analysis.

Synapse detection. For the present purposes, we define 'synapse type' as a specific combination of synaptic proteins. For example, a GABAergic (inhibitory) synapse type is defined by the presence of the general presynaptic marker, synapsin; the postsynaptic marker of inhibitory synapses, gephyrin; and the presynaptic marker of inhibitory synapses, GAD. A glutamatergic (excitatory) synapse is defined by the presence of the general presynaptic marker, synapsin, and the postsynaptic marker for excitatory synapses, PSD-95. A glutamatergic synapse with VGluT2 and adjacent to an astrocytic process is defined by the presence of synapsin, VGluT2, PSD-95, and GS, a marker for astrocytes.

Detecting synapses by their molecular composition is the first step of the computational pipeline. In order to quantitatively analyze large array tomography volumes, it is vital to find an appropriate synapse detection technique. The majority of published synapse detection methods use traditional machine learning approaches[43,46–48]. These approaches all consist of a few common steps to detect synapses. First, for each synapse type, a large number of synapses are manually identified and labeled in the array tomography data. Next, a classifier (such as a support vector machine or convolutional neural network) is trained with these manual annotations. Lastly, the entire dataset is appropriately parcellated and potential synapses are labeled by the classifier. While this method works well for certain questions in synapse biology, the difficulty in manually labeling different synapse types in immunofluorescent data renders it ineffective for our applications.

The probabilistic synapse detection method introduced in[43], is a synapse type focused approach which does not require any training data, making it a viable option for exploring synapses imaged via array tomography. 'Synapse type' focused means the user specifies the molecular composition and the relative spatial arrangement along with the size of the synaptic markers prior to running the probabilistic synapse detection method. The combination of a user-defined synapse type and marker size is called a 'query', as highlighted in Fig. 1.

A query to detect a glutamatergic synapse would look like the following: a PSD-95 punctum of a minimum of $2\,px \times 2\,ps \times 2\,slices$ (which is $0.2\,\mu m \times 0.2\,\mu m \times 0.14\,\mu m$ for our data) adjacent to a synapsin punctum of the same size. Adjacency in this case means that the puncta of the two different antibody markers do not occupy the same space but instead are juxtaposed with each other, i.e., occupy immediately adjacent pixels or share a small proportion of pixels. Since PSD-95 is a postsynaptic protein and synapsin is presynaptic protein, this simple glutamatergic synapse query follows the known biological model for glutamatergic synapses. In[43], the query comprises only
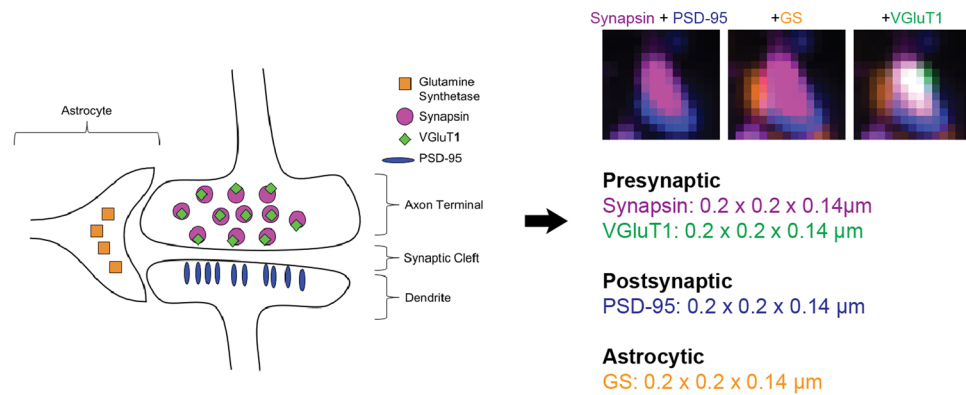
Figure 1. Outline of a query. The cartoon on the left side shows the relative spatial arrangement of the different fluorescent markers used to detect an excitatory synapse expressing VGluT1, next to an astrocyte process. This visual description of a synapse is translated into a query, shown to the right of the large black arrow. A query is a user-defined description of what the synapse type of interest should 'look' like. In this case, the presynaptic protein markers - synapsin and VGluT1, are expected to colocalize (occupy the same 3D space) with each other. Furthermore, the presynaptic, postsynaptic, and astrocyte markers (as a group) are all expected to be next to each other. The top right portion of the figure shows three $1.5\,\mu m \times 1.5\,\mu m$ cutouts of different marker combinations showing what the query looks like in the data. The first cutout shows the synapsin and PSD-95 punctum overlaid; the second cutout includes the GS punctum and the third cutout includes the VGluT1 punctum.
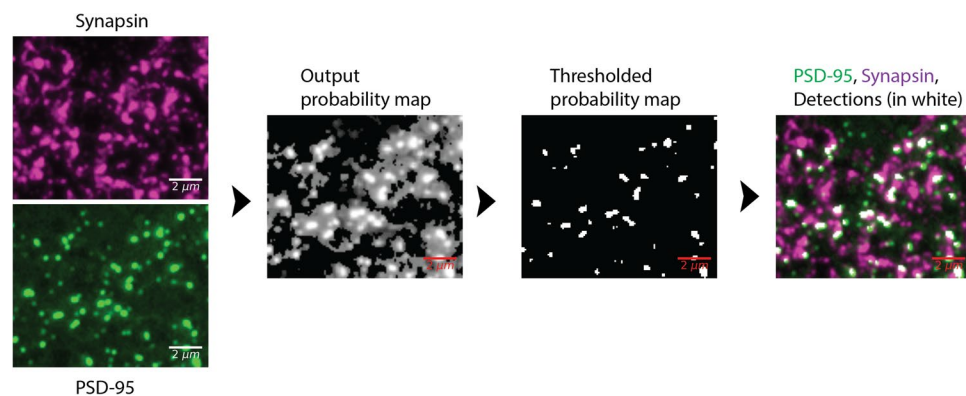

Figure 2. Probabilistic synapse detection pipeline. The first column shows the raw PSD-95 and synapsin data. The second column shows the output of the synapse detection method, where the value at each pixel is the probability that pixel belongs to the specified definition of a synapse. The third column shows the results of thresholding the output probability map. From our past work, we determined an empirical threshold of 0.9 to be the optimal value. The forth column shows the detections (in white) overlaid upon the superposition of the PSD-95 and synapse data. For this visualization, the definition of a synapse was the adjacency of a PSD-95 and synapsin punctum of a minimum size of $0.2\,\mu m \times 0.2\,\mu m \times 0.07\,\mu m$ which corresponds to $2\,px \times 2\,px \times 1\,slice$. Adjacency is defined as two puncta occupying immediately adjacent pixels, or sharing a small proportion of the pixels.

of presynaptic and postsynaptic makers. In this work, we have expanded the query to comprise of presynaptic, postsynaptic, and astrocytic markers. This combination of markers is often referred to as a 'tripartite synapse'[46]. As the left side of Fig. 1 shows, the tripartite synapse model assumes that the molecular markers for each 'subclass' (presynaptic, postsynaptic, astrocytic) lie adjacent relative to each other.

In summary, the probabilistic synapse detector is a method of detecting specific synapse types. Instead of requiring the user to manually annotate multiple instances of a synapse type to train a machine learning classifier, the query-based approach asks the user to define a synapse by specifying basic characteristics, that is, the requisite markers, requisite punctum volume for each marker (which depends on the microscope known resolution), and their relative spatial arrangement.

Once the query has been established, the probabilistic synapse detection method follows the query to automatically detect synapses matching the query. Figure 2 shows an example pipeline going from the raw input data to the thresholded synapse detections. Briefly, synapses are detected in IF-AT data through a series of steps. First, the user defines what the detection should look like. For example, it should consist of a synapsin punctum and PSD-95 punctum that lie adjacent to each other and each punctum should be at least two pixels by two

Synapse Type	Presynaptic Markers	Postsynaptic Markers	Astrocyte Marker
Glutamatergic	Synapsin	PSD-95	None
Glutamatergic VGluT1	Synapsin, VGluT1	PSD-95	None
Glutamatergic VGluT2	Synapsin, VGluT2	PSD-95	None
Glutamatergic VGluT1/VGluT2	Synapsin, VGluT1, VGluT2	PSD-95	None
GABAergic	Synapsin, GAD	Gephyrin	None
Glutamatergic adjacent to astrocyte	Synapsin	PSD-95	GS
Glutamatergic VGluT1 adjacent to astrocyte	Synapsin, VGluT1	PSD-95	GS
Glutamatergic VGluT2 adjacent to astrocyte	Synapsin, VGluT2	PSD-95	GS
Glutamatergic VGluT1/VGluT2 adjacent to astrocyte	Synapsin, VGluT1, VGluT2	PSD-95	GS
GABAergic adjacent to astrocyte	Synapsin, GAD	Gephyrin	GS

Table 2. Queries used for this analysis.

pixels by two slices. The synapse detection method uses this information to compute an output probability image. The value at each pixel is the probability it belongs to the definition of a synapse. These output images are then thresholded, resulting in synapse detections. The details of the synapse detection method are described in[43] and its applications to antibody characterization are studied in[44]. Both report extensive validation, indicating that the tool is ready to address the novel biological questions in this work.

Synapse type and size definitions. For the analysis presented in this work, we used the queries listed in Table 2. A synapse of a particular type is defined as having the relevant markers, with all the markers being of the specified size. For this study, we required the markers to span one or more slices, depending on the desired synapse size, and have a minimum x, y size of $0.2\,\mu m \times 0.2\,\mu m$. The one exception is the definition of VGluT2 synapses where the VGluT2 marker is required to span two or more adjacent slices. This is due to the properties of the VGluT2 antibody, which in addition to the expected robust label of a synapse subpopulation, also gives higher, randomly distributed, background signal (see Supplemental Table S2 for more information).

The sizes of the detected synapses followed the expected log-normal distribution[47] (Supplemental Fig. S1). For the analysis, each synapse type was further subdivided in three sizes: small, medium, and large. A small synapse is defined as having at least one of the markers on only one slice, a medium synapse is defined as having at least one of the markers on two slices and the rest of the markers on two or more slices, and a large synapse is defined as having all of the markers on three or more slices. To calculate the synapse density of small synapses, a query where synaptic markers span two or more slices is subtracted from a query where synaptic markers span one or more slices. In the same vein, to calculate the synapse density of medium synapses, a query where synaptic markers span three or more slices is subtracted from a query where the synaptic markers span two or more slices. 'All synapses' of a type are defined as having synaptic markers that span one or more slices. An important clarification needs to be made about this synapse size grouping. The detection of synapse markers is based on immunoreactions and is therefore subject to the limitations of antibody use. The absence of immunoreactivity does not equal the absence of the marker, it only indicates that the marker is below detectable levels. Therefore, a small synapse with synapsin label on only one slice does not equal a synapse with a presynaptic bouton confined within the volume of one section of $70\,nm$, rather, this is a synapse with detectable levels of synapsin on only one section.

Volume calculation. Synapse density is calculated as the number of synapses detected in a dataset over the volume of the dataset. The volume of the dataset is defined by the volume of the neuropil (i.e., excluding the volume occupied by cell nuclei and large blood vessels, which can vary significantly between areas). When choosing the areas to image, we avoided large blood vessels. To calculate the volume of cell nuclei, the nuclear stain DAPI was converted into probability space using the methods outlined in[44]. Briefly, the value at each pixel in probability space is the probability it belongs to the foreground, with a range of 0 to 1. To do so, the background noise is modeled and the foreground probability is one minus the probability the pixel belongs to the background. The background noise is modeled as a Gaussian, for which the mean and variance are calculated from the raw data itself. Once the probability map is calculated, it is thresholded (t = 0.6, chosen by observation) and cleaned up by a sequence of morphological operations. The code is available for download on the project's website. In summary, the volume of the neuropil was obtained by subtracting the volume of the DAPI stained nuclei from the total imaged volume.

Colocalization analysis. To examine the spatial relationships between glial and postsynaptic markers, we used the Colocalization test in Fiji[45], applying the van Steensel method of randomization[48]. For each pair of channels, we used a $40 \times 26\,\mu m$ region of interest through the image stack. The excitatory and inhibitory presynaptic/postsynaptic marker pairs, VGluT1/PSD95 and GAD/Gephyrin were used for comparison.

Statistical analysis. Statistical analysis to determine significance between the two populations was done via a two-tailed unpaired t-test, shown to be applicable to very small sample sizes[49], such as used in this study (n = 4). Because of the potential problems with any small sample statistical test, we are also presenting the data from each individual sample in the supplemental figures section. Plots showing the data for each synapse type, size, and layer are found in Supplemental Figs S2, S3, S4, S5, S6 and S7. Alternative statistical analysis could be carried out with the data and code we publicly provide.

Results

We used immunofluorescent array tomography (IF-AT) to quantify the synaptic density, composition and glial involvement in layers 1 through 4 of the somatosensory cortex of adult FMR1 knockout (KO) mice and wild-type (WT) mice. IF-AT is based on digital reconstruction of images acquired from arrays of serial ultrathin sections (70 nm) attached to coverslips, immunofluorescently labeled and imaged under a fluorescence microscope. The use of ultrathin sections allows the light level detection of individual synapses, while the possibility of applying multiple immunofluorescent markers (10 or more) enables the identification of different synaptic populations[41]. Synaptic density was quantified using automatic synapse detection methods previously developed by our group[43,44]. Besides the already published validation of our method, results from WT mice were also compared to available estimates in the literature as an additional control.

Overview of the datasets and detected synapses.   Volumes of approximately $140 \times 400 \times 2.7 \, \mu m$ spanning layers 1 through 4 of the somatosensory cortex of FMR1 KO mice and WT mice were imaged, as shown in Fig. 3. We detected an average of 200,000 synapses in each volume for a total of approximately 1.6 million synapses across all eight datasets. Excitatory synapses were identified by the presence of immunofluorescent signals from both synapsin, a presynaptic protein, and PSD-95, a protein of the postsynaptic scaffold of excitatory synapses. Excitatory synapses were further subdivided depending on their vesicular glutamate transporters into VGluT1 positive, generally thought to be of intracortical origin, and VGluT2 positive, belonging predominantly to thalamocortical inputs[28,29,50]. Inhibitory synapses were identified by the presence of the general presynaptic marker synapsin and the presynaptic marker for GABAergic synapses, glutamic acid decarboxylase (GAD), together with the postsynaptic marker gephyrin. Astrocytes, including their processes, were detected using an antibody against glutamine synthetase (GS)[51,52], which allowed for the identification of the fraction of synapses that are immediately adjacent to astrocytic processes. In addition to identifying synapses based on combinations of different markers, synapses were also analyzed based on their size, because size is known to correlate with the maturity and strength of a synaptic connection. Newly formed synapses tend to be small, and at mature synapses the size of the postsynaptic density is known to correlate well with synaptic strength[53]. Visual inspection of the datasets did not uncover any obvious differences in immunofluorescence intensity and pattern for any of the markers between the KO and WT mice. The cortical thickness was also comparable between the two conditions ($0.88 \pm 0.03 \, mm$ for KO vs. $0.89 \pm 0.02 \, mm$ for WT, $p = 0.71$).

Single channel analysis.   We first quantified the puncta density of the different synaptic markers in the KO and WT mice. This is a rather crude analysis, especially for the small puncta which are present on only one slice and therefore potentially include nonspecific label. However, these results provide an overview of the data and also serve to highlight the importance of the subsequent synapse detection as a much more reliable tool for monitoring synaptic changes. Quantification of the puncta density of the different synaptic markers did not reveal any statistically significant differences ($p > 0.05$) when averaging Layers 1–4, as shown in Fig. 3B and in more detail in Supplemental Fig. S2. There was a tendency for a decrease in the number of small VGluT2 puncta ($p = 0.065$) and large PSD95 puncta ($p = 0.065$). On the other hand, medium PSD-95 puncta tended to increase ($p = 0.056$), as shown in the middle panel of Fig. 3.

The only significant change that was detected was in the density of GS puncta of different sizes: in FMR1 KO mice there were more small puncta ($p = 0.01$), as well as a tendency for a decrease in the number of large GS puncta ($p = 0.07$), as shown in the bottom panel of Fig. 3.

Even though we did not detect any significant changes in the densities of puncta of the different synaptic markers, this does not necessarily preclude changes in the synaptic populations of FMR1 KO mice. The synaptic proteins assessed in our study are indeed highly enriched at synapses, but they are also found at extra-synaptic sites, and thus their presence does not necessarily equate to the presence of a synapse.

Overall synapse densities.   A much more accurate detection of synapses is achieved by using combinations of synaptic makers, ideally at least one presynaptic and one postsynaptic marker, as specified by our synapse detection algorithm[43,44]. Indeed, using such combinations of synaptic markers, the detected synapse densities and distributions in WT mice are consistent with previous estimates as shown in Fig. 4. The overwhelming majority of cortical synapses are known to be either excitatory glutamatergic or inhibitory GABAergic synapses[54]. Thus, the total density of synapses was estimated by the sum of the densities of the detected glutamatergic (synapsin + PSD95 markers) and GABAergic synapses (synapsin + GAD + gephyrin markers) resulting in approximately 1.94 synapses per μm^3 of embedded tissue. Because tissue dehydration and embedding with our protocol result in approximately 23% linear shrinkage, or 54% volumetric shrinkage[55], this equals to 0.9 synapses per μm^3 of unprocessed tissue, very similar to the reported synapse density in mouse cortex[56].

The relative contributions of inhibitory and excitatory synapse types that we detect are consistent with the known synapse composition of mouse cortex. The percent of inhibitory GABAergic synapses in our detections varies between 12% in layer 1 to 20% in layer 4 (Fig. 4F). Electron microscopy (EM) counts in mouse somatosensory cortex show that inhibitory synapses consist of 11% of the synapses in layer 1[57] and 18% of the synapses in layer 4[58].

The layer distribution of VGluT2 synapses is consistent with their known preference for layer 4 (Fig. 4G). VGluT2 is known to label thalamocortical synapses which target mostly layer 4 and lower layer 2/3[59,60]. Thalamocortical synapses, identified either by degeneration techniques, anterograde transport of lectin, or VGluT2 immunostaining, have been shown to comprise approximately 20% of glutamatergic synapses in layer 4 of mouse somatosensory cortex[61-63] and we indeed see 21% in layer 4.

To further verify the accuracy of our detections, we used a different way to calculate the density of excitatory glutamatergic synapses. These synapses can be subdivided into two major populations depending on the
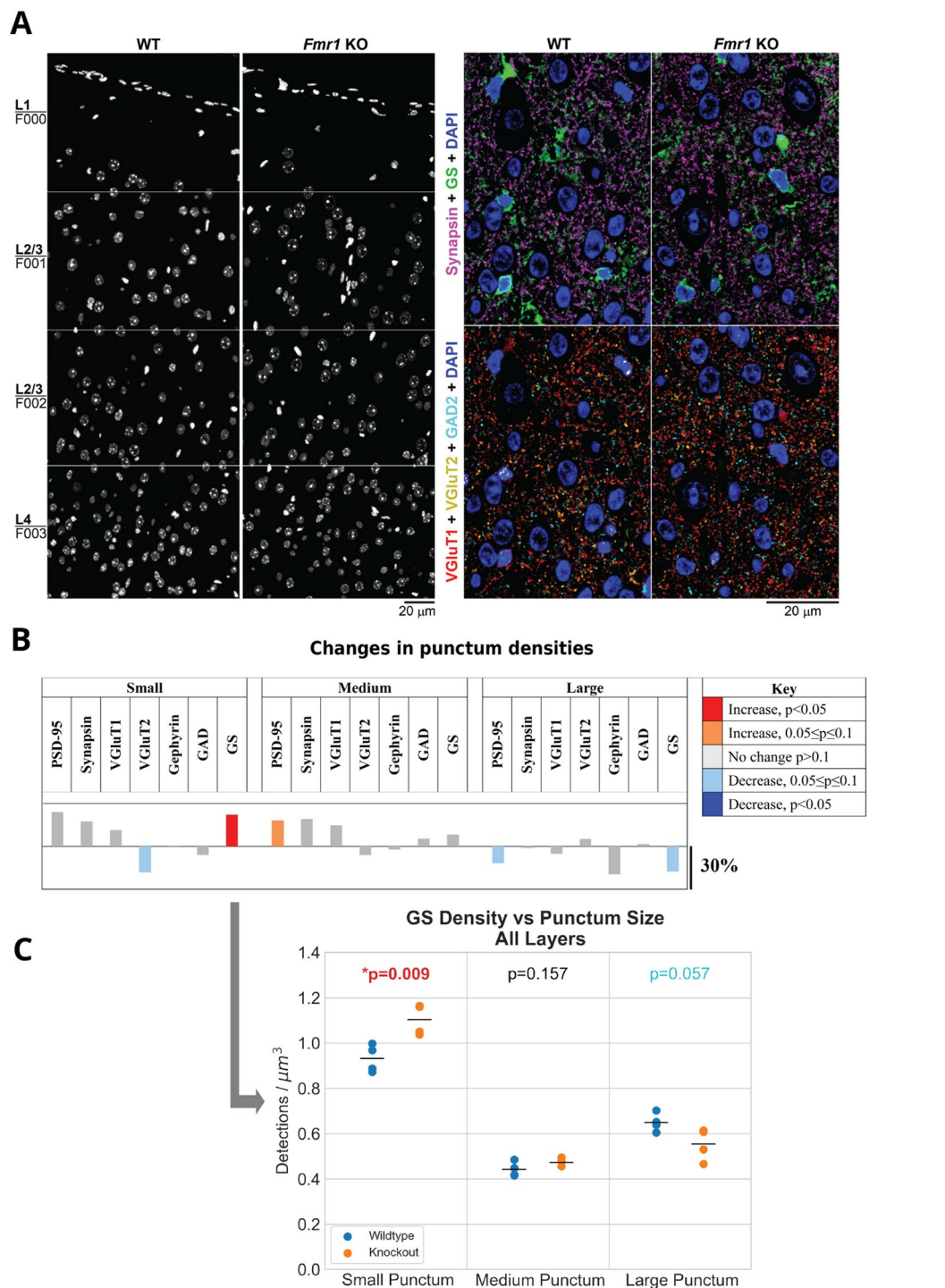
Figure 3. Overview of the datasets. (**A**) Immunofluorescent array tomography of wild-type and FMR1 knockout mouse somatosensory cortex. The left panel shows the imaged area in each sample, consisting of four tiles spanning cortical layers 1 through 4. DAPI staining of nuclei, volume reconstruction of 30 serial sections, 70 nm each. The right panel shows the immunofluorescence for synaptic (synapsin, VGluT1, VGluT2 and GAD2) and glial (GS) markers in wild-type and knockout mouse somatosensory cortex layer 4, volume reconstruction of 10 serial sections, 70 nm each. (**B**) Summary of single channel punctum density changes between wild-type and knockout mice with all layers averaged. The plots show the percentage difference between the wild-type and knockout mice and are color-coded to indicate direction of change and statistical significance. (**C**) This plot shows the density distribution of GS puncta by size. 'Small' puncta span one slice, 'medium' puncta span two slices, and 'large' puncta span three or more slices.
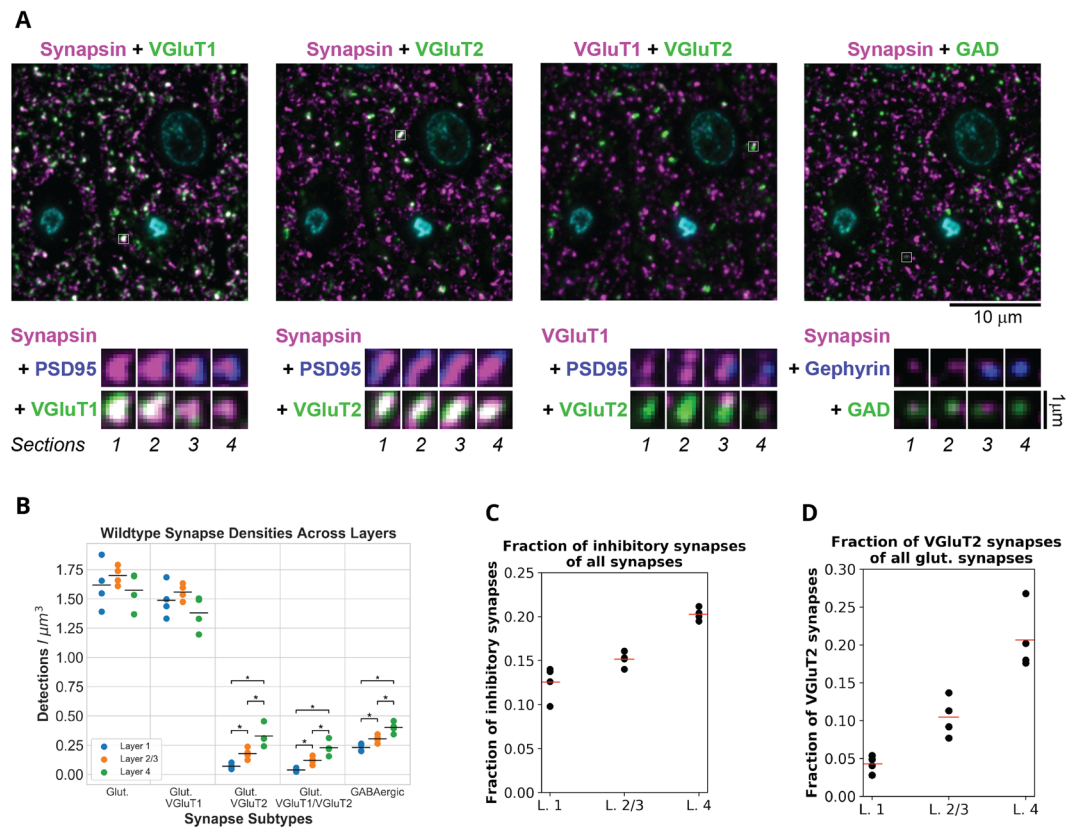
Figure 4. Overview of wild-type synapse density distributions. (**A**) Top, multiplexed immunofluorescence from the same area of a single section of the somatosensory cortex of a WT mouse. The nuclear stain DAPI is in cyan. White squares highlight individual synapses, which in A, bottom, are shown at higher magnification on 4 consecutive serial sections. (**B**) The distribution of synapse types across different layers. Layers with significant differences for a synapse type are marked. While there is no significant difference in layer densities for glutamatergic synapses overall and for glutamatergic synapses with VGluT1, there is a significant difference between layers for glutamatergic synapses with VGluT2, with both VGluT1 and VGluT2, and for inhibitory synapses. (**C**) Fraction of inhibitory synapses in layers 1 through 4 of mouse somatosensory cortex. (**D**) Fraction of VGluT2 synapses in layers 1 through 4 of the mouse somatosensory cortex.

	Glut	VGluT1 + VGluT2-VGluT1/2
L1	1.617	1.629
L2/3	1.700	1.750
L4	1.574	1.585

Table 3. Density distribution of excitatory synapses across layers as calculated by two methods. Units are number of synapses per cubic micron.

vesicular glutamate transporters (VGluTs) at the presynaptic site, with the majority of excitatory synapses containing VGluT1, and a smaller population, mostly concentrated in layer 4, VGluT2. In addition, some synapses express both VGluT1 and VGluT2[64]. Thus, the density of glutamatergic synapses should be approximately equal to the densities of VGluT1 and VGluT2 synapses minus VGluT1/VGluT2 synapses to prevent double counting of the same synapse. This was indeed the case, as seen in Table 3.

Changes in synaptic densities in FMR1 KO mice. Next, we compared the densities of the different synapse populations in the WT mice to the FMR1 KO mice. Even though the individual synaptic marker puncta did not show any statistically significant differences in the two conditions, there were wide-ranging changes in synaptic densities. These changes were dependent on the synapse type, size, as well as cortical layer, as shown in Fig. 5 and in more detail in Supplemental Fig. S3. There was an increase of small glutamatergic VGluT1 synapses in layer 4 accompanied by a decrease in large VGluT1 synapses in layers 1 and 4. VGluT2-containing synapses, on the other hand, showed a rather consistent decrease in density in layers 1 and 2/3. Large inhibitory synapses decreased across all layers examined without detected changes in small and medium size inhibitory synapses.

These changes in density of the various synaptic populations resulted in an increase in the excitation-inhibition ratio in the FMR1 KO mice, consistent with previous reports: 6.20 ± 0.56 for the KO vs. 5.24 ± 0.32 in WT (average
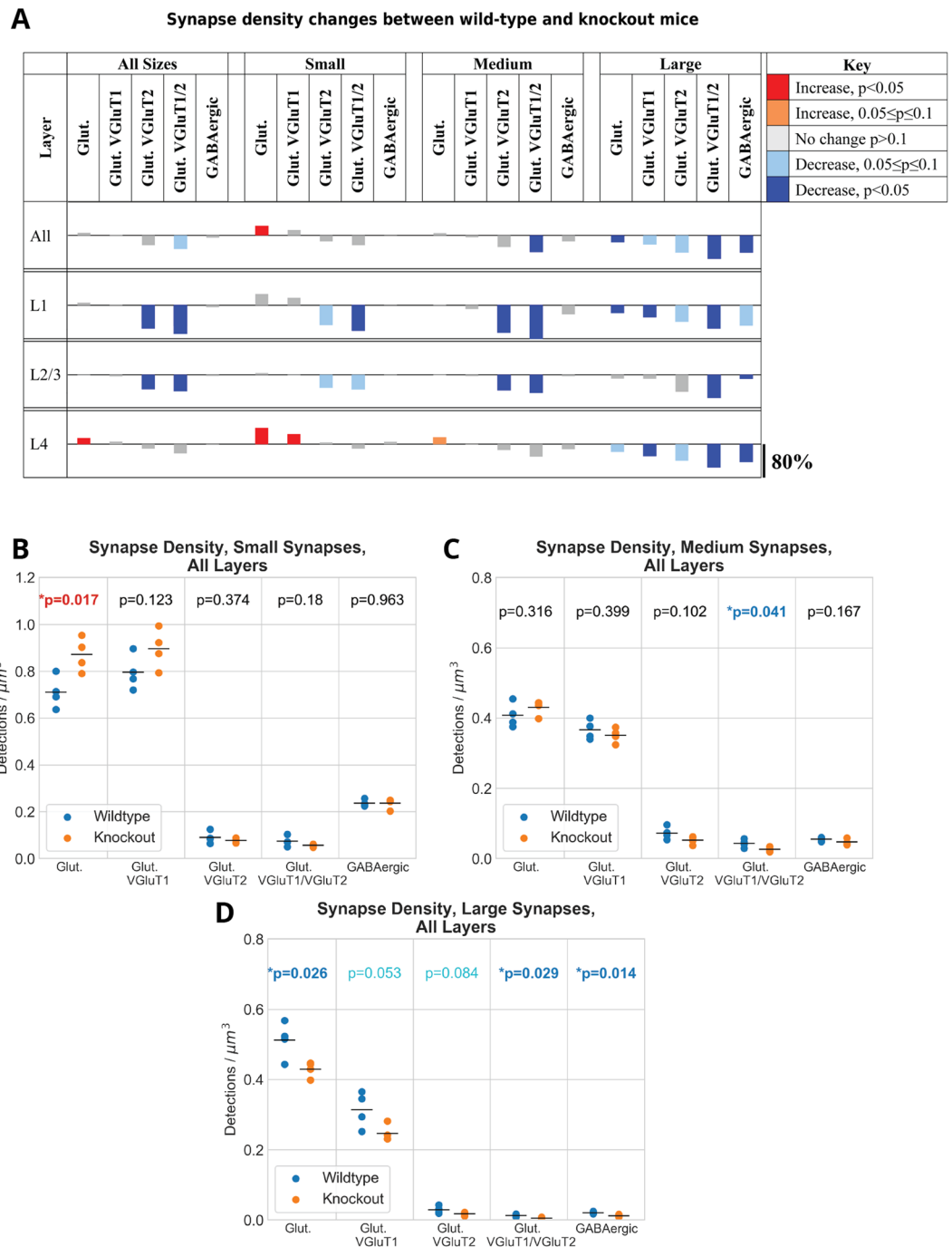
Figure 5. Changes in synapse densities across layers. (**A**) Summary table showing the synapse types that have a significant increase or decrease in synapse density between wild-type and knockout mice. Each row shows plots of the percentage difference in density between the wild-type and knockout mice. Plots are color-coded to indicate direction of change and statistical significance. (**B**–**D**) Differences in synapse density for different synapse types for three expected synapse sizes.

for layers 1 through 4; $p = 0.04$). Similar increase was observed in all examined layers, but it did not reach statistical significance. Excitation was defined by the number of synapses which contain synapsin and PSD95, and inhibition by the number of synapses containing synapsin, GAD and gephyrin. These changes are highlighted in Fig. 6G.

Because the strength of excitatory synapses is known to be proportional to the size of the postsynaptic density, we also analyzed the changes specifically at the postsynaptic side as shown in Fig. 6A–F and in more detail in Supplemental Fig. S4. There was a statistically significant increase in the density of glutamatergic and specifically VGluT1 synapses with small PSD-95 puncta (spanning only 1 or 2 slices), and a significant decrease in the density of the VGluT2 synapses with large PSD-95 puncta (spanning 6 or more slices). No changes in the densities of inhibitory synapses depending on the size of gephyrin puncta were detected, as shown in more detail in Supplemental Fig. S5.
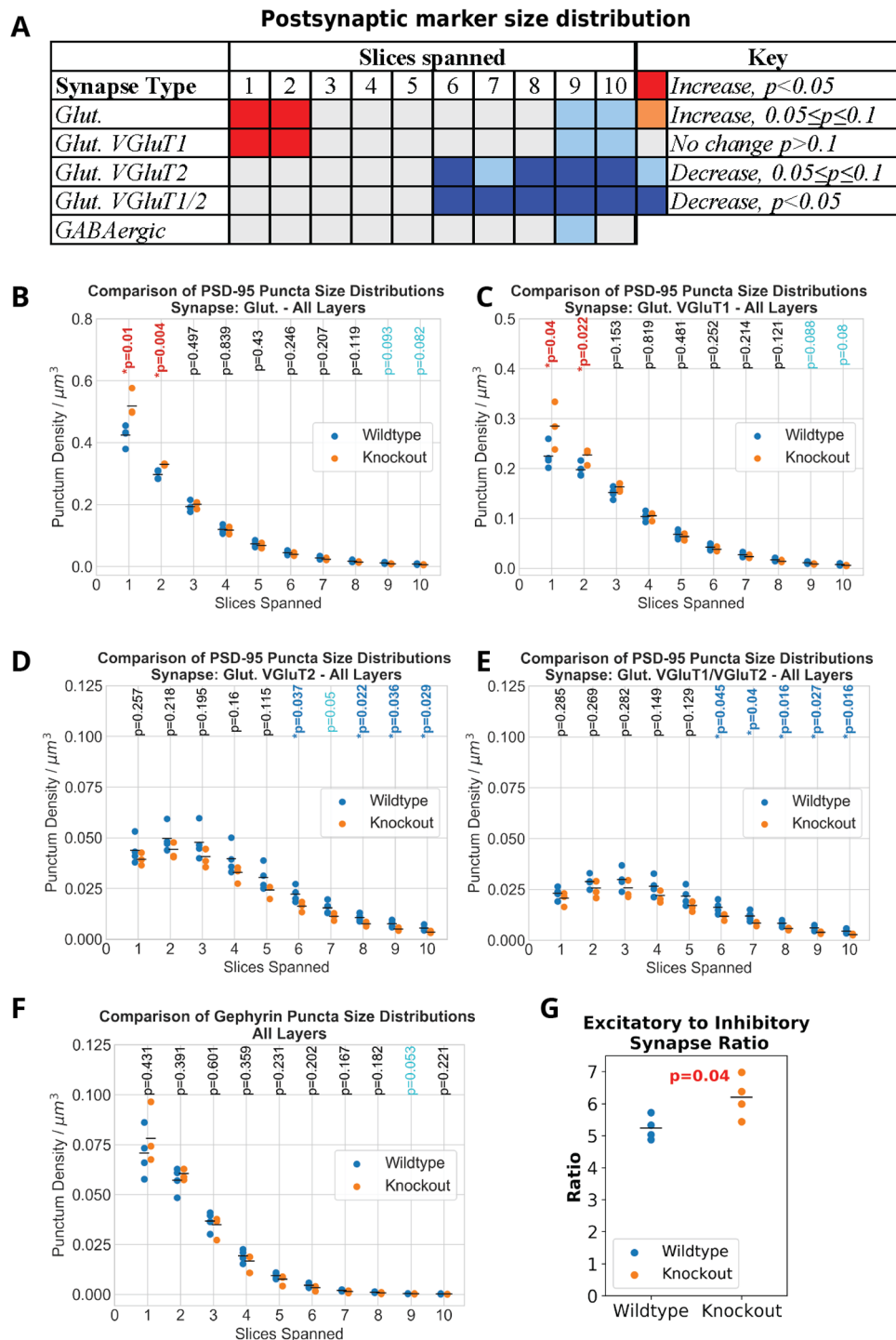
Figure 6. Postsynaptic marker size distributions. (**A**) Summary table showing the differences in the size distributions of PSD-95 puncta associated with synapses by type. The main takeaway is that for excitatory synapses overall, there is an increase in the number of small PSD-95 puncta in FMR1 knockout mice while there is a decrease in the number of very large PSD-95 puncta associated with synapses containing VGluT2. (**B–E**) Plots showing the distribution of PSD-95 puncta for both wild-type and knockout mice. (**F**) Size distribution of gephyrin puncta associated with inhibitory synapses. (**G**) Plot shows the significant increase in the ratio of excitatory to inhibitory synapses in knockout mice.

Involvement of glia (astrocytes). Astrocytes are intimately involved in synaptic function and their processes are found adjacent to many synaptic clefts in the neocortex. Because astrocytes in the mouse also express FMRP[34] and are suspected to have a role in FXS pathogenesis[36], we analyzed the potential changes in astrocytic involvement at synapses in the FMR1 KO mice. Astrocytes were detected using antibodies to glutamine
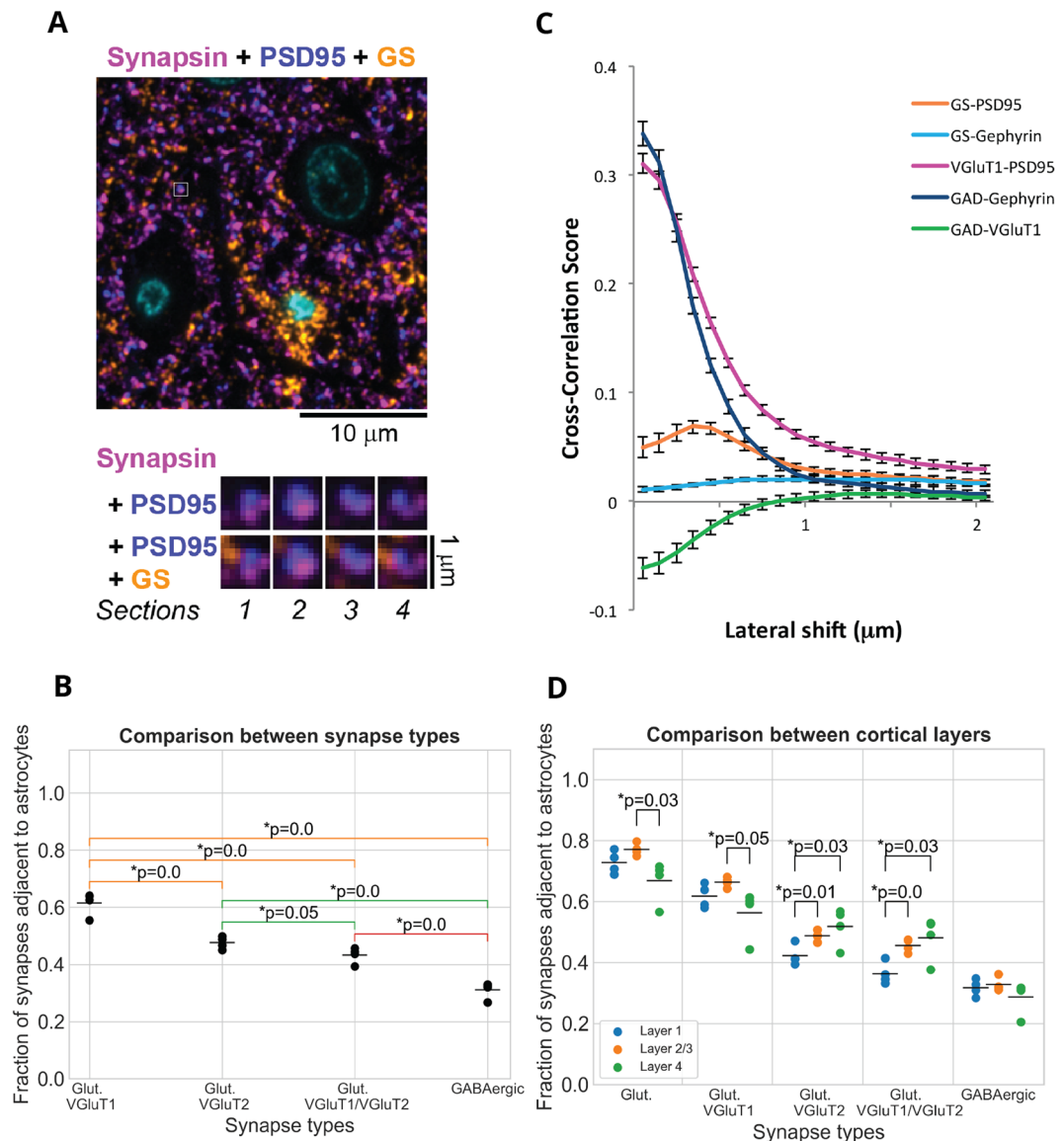
Figure 7. Astrocytic association of synapses in wild-type mice. (**A**) Portion of the wild-type synapse data with a synapse highlighted with a white box. Below are serial sections through the highlighted synapse, shown at higher magnification. (**B**) The fraction of synapses associated with astrocytes varies depending on synapse type. (**C**) Cross-correlation score as a function of lateral offset between the two channels. The synaptic marker pairs VGluT1 - PSD-95 and GAD - Gephyrin are shown for comparison. The correlation between the synaptic markers is high with no shift and it drops off sharply with lateral offset, as expected for tightly correlated presynaptic and postsynaptic markers. On the other hand, GAD and VGluT1 do not colocalize, because they label different synapse types, and the negative colocalization score with no shift gradually increases to 0 with lateral offset. (**D**) Between layer differences in the astrocytic association of different synapse types.

synthetase, an enzyme known to be expressed predominantly by this cell type[51,52] and specifically found at the peripheral astrocytic processes that contact synapses[65,66]. Figure 7A shows an example of the data.

In wild-type mice, we found that the majority of glutamatergic synapses ($72 \pm 2\%$) are adjacent to astrocytic processes as detected by immunolabel to glutamine synthetase. This is very similar to previous EM estimates in mouse somatosensory cortex layer 4, where 68% of glutamatergic synapses on dendritic spines were in contact with astrocytic processes at the bouton-spine interface[67]. The proportion of glutamatergic synapses in contact with astrocytes was not uniform across layers, and we detected the highest association in layer 2/3 (Fig. 7D), similarly to previous observations in rat visual cortex[68]. Interestingly, we observed significant differences in the astrocytic association of the different synapse types, as shown in Fig. 7B. Thus, compared to the majority glutamatergic synapses containing VGluT1 ($61 \pm 2\%$ astrocytic association), significantly less VGluT2 synapses ($46 \pm 1\%$, $p < 0.001$) were adjacent to astrocytes. The difference in astrocytic association was even more pronounced when considering the inhibitory GAD synapses which were half as likely to be adjacent to an astrocytic process ($29 \pm 1\%$, $p < 0.001$) compared to excitatory VGluT1 synapses.

Because there are no previous data about differences in glial association of cortical excitatory and inhibitory synapses, we sought additional evidence to confirm this finding. We quantified the colocalization between the astrocytic marker (GS) and the postsynaptic markers for excitatory (PSD95) and inhibitory (gephyrin) synapses using the van Steensel method[48]. This method evaluates the extent of spatial correlation by testing for the effect of very small relative displacements between pairs of marker images on a measurement of image overlap, the Pearson correlation coefficient. Because of the abundance of synaptic and glial markers, overlapping spatial distributions might occur by chance. If the association between two channels is real, however, then any shift of one channel relative to the other will decrease the observed degree of colocalization. On the other hand, if two channels tend to be mutually exclusive, then a shift will increase the degree of colocalization. Finally, if the association between two channels is occurring by chance, then a shift will not substantially affect the degree of colocalization. Because this analysis was performed on volumes containing several thousand synapses, which in cortex have random orientations, the change in the degree of colocalization between two channels does not depend on the direction of the shift, but only on its size. Consistent with our findings with the probabilistic synapse detector, the van Steensel method detected a colocalization between the astrocytic marker GS and the postsynaptic excitatory marker PSD95 (Fig. 7C). The degree of colocalization increased with shifts between the two channels of up to 0.3–0.4 μm, suggesting that the two markers are adjacent, but not overlapping. No colocalization was detected between GS and the postsynaptic inhibitory marker gephyrin. This does not mean that GS was not present next to a portion of inhibitory synapses, it only signifies that GS was not preferentially associated with inhibitory synapses. This result is consistent with our finding that excitatory synapses are more likely to be associated with astrocytic processes compared to inhibitory synapses.

Comparison of WT with KO mice revealed a number of significant changes in astrocytic involvement at synapses. Consistent with the detected overall changes in synaptic density, there were significant decreases in the densities of synapses adjacent to astrocytes, for almost all synapse types and sizes as shown in Fig. 8A and in more detail in Supplemental Fig. S6. The only exception were the small glutamatergic synapses in layer 4, for which the density of synapses adjacent to astrocytes increased in KO mice. While the density of synapses adjacent to astrocytes is very much influenced by the changes in overall synaptic density, the fraction of synapses adjacent to astrocytes reflects the actual changes in glial involvement in Fragile X Syndrome. There was an overall decrease in the fraction of synapses adjacent to astrocytes for all synapse types and layers, but the differences did not reach statistical significance in many cases, likely due to the large variability within each genotype. A significant decrease in the fraction of synapses adjacent to astrocytes was detected for glutamatergic and VGluT1 synapses of all sizes, except small VGluT1 synapses (layers 1–4 combined) as shown in Fig. 8B and in more detail in Supplemental Fig. S7. When analyzed by cortical layer, there were significant decreases in the fraction of astrocytic association for large glutamatergic synapses in layers 1 and 2/3, large VGluT1 synapses in layer 1, small and medium VGluT2 synapses in layers 2/3, and medium GAD synapses in layer 1.

Discussion

Using immunofluorescent array tomography and automatic probabilistic synapse detection methods we show wide-ranging changes of synapses and their association with astrocytes in the somatosensory cortex of adult FMR1 knock-out mice, a Fragile X mouse model. Overall, there is a significant decrease in the density of excitatory glutamatergic synapses and their association with astrocytes. However, the changes vary greatly, and are at times in opposite directions, depending on synapse type, size, as well as cortical layer. The changes in supragranular layers (layers 1 and 2/3) reflect the overall decrease in the density of glutamatergic synapses, predominantly of the VGluT2 type. Meanwhile in the granular layer (layer 4) there is a slight but significant increase in the density of glutamatergic synapses, resulting from an increase in small VGluT1 synapses, offset by a decrease in large VGluT1 synapses. The astrocytic association of excitatory synapses decreases. As for the inhibitory GABAergic synapses, there is a consistent decrease in the density of large synapses in all examined layers, and a decrease in the astrocytic association of medium-sized synapses in layer 1. The overall loss of inhibitory synapses is greater than for excitatory synapses, suggesting a potential shift in the excitation/inhibition ratio toward greater excitation in FMR1 knock-out mice. Thus, the absence of FMRP markedly alters the neocortical synaptic circuitry by both changing the relative contributions of synapses of different types, and the astrocytic involvement at synapses.

Our results are consistent with reported data in adult FMR1 knock-out mice suggesting cortical circuit changes such as increase in smaller size immature synapses and decrease in larger size synapses (as evidenced by the spine size in[35,69]), as well as decreased association of astrocytes with hippocampal synapses[35]. We have extended these observations, by showing that these changes are not uniform, but depend on the synapse type, as well as cortical layer. A previous study had indeed shown that layers 4 and 5 synapses of different types in mouse somatosensory cortex exhibit various deficits in FMR1 knock-out mice[31] and we have now characterized the synapse type specific changes in the supragranular layers as well. Finally, we are showing for the first time a decrease in astrocytic involvement at neocortical excitatory glutamatergic synapses, most pronounced at medium and large size synapses.

A potential caveat of our study is the small number of analyzed animals, due to the laborious nature of these experiments. In order to minimize variations between experimental sessions and obtain more accurate results, our original design was to immunolabel and image the samples in pairs, one KO and one WT. The subsequent analysis revealed good consistency from experiment to experiment, as evidenced by the individual data points presented in the Supplemental figures, which enabled the detection of multiple synaptic changes in the FMR1 KO mice regardless of the small number of animals. In addition, comparison of our results from WT mice to the available published data, further confirmed that we are not only able to correctly quantify the densities of the two main synapse types, excitatory and inhibitory, but that we are also detecting the known layer variations in VGluT2 synapses[61–63], and even the rather subtle layer variations in astrocytic association of excitatory synapses[68].
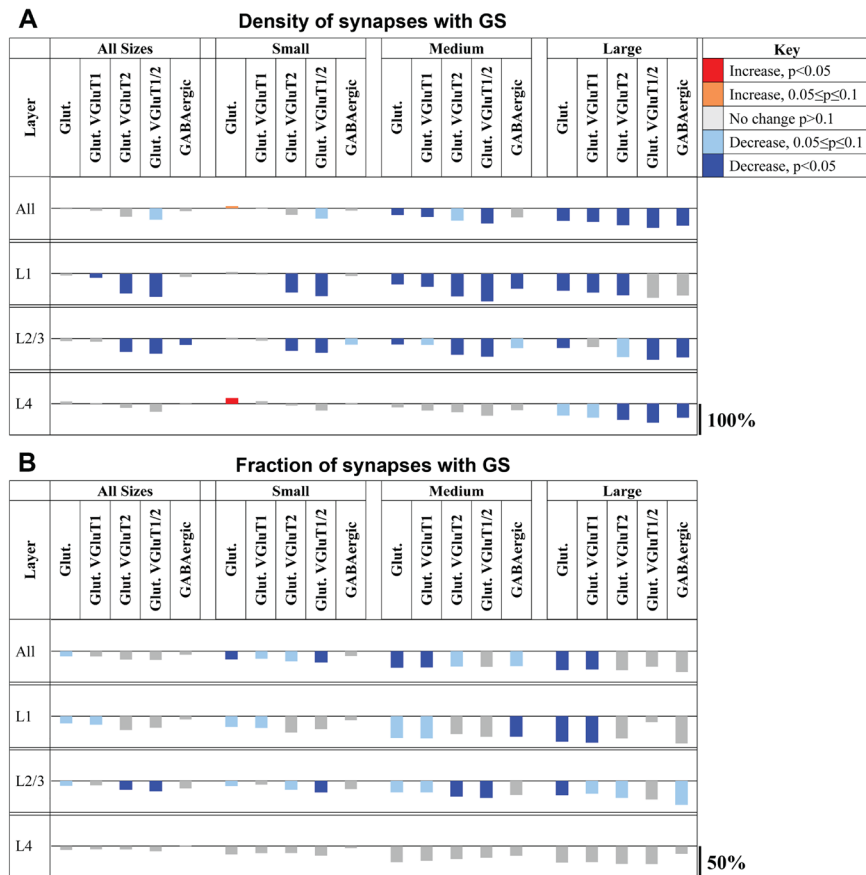
Figure 8. Summary of the astrocytic synapse density differences in the knockout mice. (**A**) Changes are shown as the percentage difference in density between the wild-type and knockout mice. Plots are color-coded to indicate direction of change and statistical significance. The density decreases between the wild-type and knock-out mice for Layers 1–3 and the difference is especially pronounced for medium and large synapses. (**B**) Changes in the fraction of synapses adjacent to astrocytic processes.

Nevertheless, the rather large variability within genotype for some of the synapse types and cortical layers likely prevented us from detecting all changes at the synapses of the FMR1 KO mice. Thus, the fact that we did not observe statistically significant changes in the astrocytic involvement at synapses in layer 4, should not be interpreted as evidence for a lack of change. Further experiments involving larger numbers of animals are needed to conclusively address this issue.

Our findings raise important questions about the implications of the observed changes in the neocortical synaptic circuitry of FMR1 KO mice. These changes are complex, involving a variety of synapse types, as well as glia. There is a shift in the size of excitatory, presumably intracortical VGluT1 synapses, manifested in the increase in small VGluT1 synapses and a decrease of large VGluT1 synapses. As synapse size is known to correlate with the strength of the synapse, this change implies a decrease in stronger VGluT1 synapses. There is also a decrease in the density of VGluT2, presumably thalamocortical synapses, also known to be strong synapses[70]. Concomitantly, there is a decrease in the astrocytic involvement at glutamatergic synapses, likely resulting in impaired glutamate uptake[71]. The combination of these changes suggests a decrease in glutamatergic signaling in the somatosensory cortex of FMR1 KO mice, arising from fewer strong intracortical and thalamocortical synapses. This might be accompanied by a loss of the acuity of those connections, since fewer closely associated astrocytes might result in more glutamate spill over at these synapses. The concomitant loss of inhibitory synapses might counteract the loss of excitatory signal strength to some extent, but might also contribute to the loss of acuity, essentially decreasing the functional signal-to-noise ratio of the circuit in FMR1 KO mice. It is known that somatosensory processing is abnormal in FMR1 KO mice[12,13], and a decreased signal-to-noise ratio could be contributing to many of the deficits, for example, to the blurred whisker maps observed in FMR1 KO mice[72,73]. Interestingly, the decrease in sensory tuning is observed in layers 2/3, but not layer 4 of FMR1 KO mouse somatosensory cortex[72], consistent with the much larger changes in the layer 2/3 synaptic circuitry that we report.

A common hypothesis regarding the functional deficits in autism focuses on the imbalance in the excitation and inhibition[74]. While our results are consistent with an increase in the excitation/inhibition ratio, they also highlight the complexity of changes that might contribute to this effect, and support the notion that the excitation/inhibition ratio is a measure that lumps together a variety of changes in the synaptic circuitry that likely have diverse functional consequences[75]. Furthermore, we also show that, in addition to synapses, there are specific deficits in cortical astrocytes and their interactions with synapses. The most pronounced changes

occur at glutamatergic synapses. Indeed, it has been shown that glutamatergic but not GABAergic neurons, critically depend on the presence of glia to establish synaptic transmission[76]. Studies employing selective deletion of FMRP in astrocytes strongly suggest the involvement of these glial cells in Fragile X pathogenesis[36], likely through impaired glutamate uptake[71]. Interestingly, the decrease in astrocytic association of glutamatergic synapses may have a different effect on VGluT1 and VGluT2 synapses and may thus contribute to the heterogeneous changes in these 2 synapse types. Thus, in developing visual cortex astrocytes have been shown to secrete hevin, a protein that stabilizes specifically VGluT2 synapses[77]. The decrease in astrocytic presence at glutamatergic synapses, and therefore decreased hevin concentration, may result in loss of some VGluT2 synapses without affecting VGluT1 synapses. It thus appears that in Fragile X Syndrome astrocytes may mediate at least some of the pathological effects on glutamatergic synapses[78–80].

Overall, our study reveals complex, synapse-type and layer specific changes in the somatosensory cortex of FMR1 knock-out mice. Some of these changes are in opposite directions, or affect only a small population of synapses and therefore become obscured when analyzing the overall synaptic content. The ability to dissect the deficits by specific synapse categories, as well as astrocytic involvement, are crucial for understanding the overall picture of synaptic changes, to begin to unravel the multiple ways in which they affect circuit function, and ultimately define targets for therapeutic treatment and prevention.

Data and Code Availability

The code and raw data are available for download at https://aksimhal.github.io/astrocytes-synapses-fxs/.

References

1. Hunter, J. *et al.* Epidemiology of fragile X syndrome: A systematic review and meta-analysis. *American Journal of Medical Genetics Part A* **164**, 1648–1658, https://doi.org/10.1002/ajmg.a.36511 (2014).
2. Berry-Kravis, E. Epilepsy in fragile X syndrome. *Developmental Medicine & Child Neurology* **44**, 724–728, https://doi.org/10.1111/j.1469-8749.2002.tb00277.x (2002).
3. Fisch, G. S., Simensen, R. J. & Schroer, R. J. Longitudinal Changes in Cognitive and Adaptive Behavior Scores in Children and Adolescents with the Fragile X Mutation or Autism. *Journal of Autism and Developmental Disorders* **32**, 107–114, https://doi.org/10.1023/A:1014888505185 (2002).
4. Penagarikano, O., Mulle, J. G. & Warren, S. T. The Pathophysiology of Fragile X Syndrome. *Annual Review of Genomics and Human Genetics* **8**, 109–129, https://doi.org/10.1146/annurev.genom.8.080706.092249 (2007).
5. Jin, P., Alisch, R. S. & Warren, S. T. RNA and microRNAs in fragile X mental retardation. *Nature Cell Biology* **6**, 1048–1053, https://doi.org/10.1038/ncb1104-1048 (2004).
6. Bagni, C. & Greenough, W. T. From mRNP trafficking to spine dysmorphogenesis: The roots of fragile X syndrome. *Nature Reviews Neuroscience* **6**, 376–387, https://doi.org/10.1038/nrn1667 (2005).
7. Bardoni, B., Davidovic, L., Bensaid, M. & Khandjian, E. W. The fragile X syndrome: Exploring its molecular basis and seeking a treatment. *Expert Reviews in Molecular Medicine* **8**, 1–16, https://doi.org/10.1017/S1462399406010751 (2006).
8. Contractor, A., Klyachko, V. A. & Portera-Cailliau, C. Altered Neuronal and Circuit Excitability in Fragile X Syndrome. *Neuron* **87**, 699–715, https://doi.org/10.1016/j.neuron.2015.06.017 (2015).
9. Wisniewski, K. E., Segan, S. M., Miezejeski, C. M., Sersen, E. A. & Rudelli, R. D. The fra(X) syndrome: Neurological, electrophysiological, and neuropathological abnormalities. *American Journal of Medical Genetics* **38**, 476–480, https://doi.org/10.1002/ajmg.1320380267 (1991).
10. Irwin, S. A. *et al.* Abnormal dendritic spine characteristics in the temporal and visual cortices of patients with fragile-X syndrome: A quantitative examination. *American Journal of Medical Genetics* **98**, 161–167, 10.1002/1096-8628(20010115)98:2<161::AID-AJMG1025>3.0.CO;2-B (2001).
11. Comery, T. A. *et al.* Abnormal dendritic spines in fragile X knockout mice: Maturation and pruning deficits. *Proceedings of the National Academy of Sciences* **94**, 5401–5404, https://doi.org/10.1073/pnas.94.10.5401 (1997).
12. Irwin, S. A. *et al.* Dendritic spine and dendritic field characteristics of layer V pyramidal neurons in the visual cortex of fragile-X knockout mice. *American Journal of Medical Genetics* **111**, 140–146, https://doi.org/10.1002/ajmg.10500 (2002).
13. Galvez, R. & Greenough, W. T. Sequence of abnormal dendritic spine development in primary somatosensory cortex of a mouse model of the fragile X mental retardation syndrome. *American Journal of Medical Genetics* **135 A**, 155–160, https://doi.org/10.1002/ajmg.a.30709 (2005).
14. McKinney, B. C., Grossman, A. W., Elisseou, N. M. & Greenough, W. T. Dendritic spine abnormalities in the occipital cortex of C57BL/6 Fmr1 knockout mice. *American Journal of Medical Genetics - Neuropsychiatric Genetics* **136 B**, 98–102, https://doi.org/10.1002/ajmg.b.30183 (2005).
15. Grossman, A. W., Elisseou, N. M., McKinney, B. C. & Greenough, W. T. Hippocampal pyramidal cells in adult Fmr1 knockout mice exhibit an immature-appearing profile of dendritic spines. *Brain Research* **1084**, 158–164, https://doi.org/10.1016/j.brainres.2006.02.044 (2006).
16. Bagni, C. & Zukin, R. S. A Synaptic Perspective of Fragile X Syndrome and Autism Spectrum Disorders. *Neuron* **101**, 1070–1088, https://doi.org/10.1016/j.neuron.2019.02.041 (2019).
17. Rudelli, R. D. *et al.* Adult fragile X syndrome - Clinico-neuropathologic findings. *Acta Neuropathologica* **67**, 289–295, https://doi.org/10.1007/BF00687814 (1985).
18. Hinton, V. J., Brown, W. T., Wisniewski, K. & Rudelli, R. D. Analysis of neocortex in three males with the fragile X syndrome. *American Journal of Medical Genetics* **41**, 289–294, https://doi.org/10.1002/ajmg.1320410306 (1991).
19. Dailey, M. E. & Smith, S. J. The dynamics of dendritic structure in developing hippocampal slices. *Journal of neuroscience* **16**, 2983–94, 1996/05/01 00:01 (1996).
20. Fiala, J. C., Feinberg, M., Popov, V. & Harris, K. M. Synaptogenesis via dendritic filopodia in developing hippocampal area CA1. *The Journal of neuroscience: the official journal of the Society for Neuroscience* **18**, 8900–11, https://doi.org/10.1523/JNEUROSCI.18-21-08900.1998 (1998).
21. Zuo, Y., Lin, A., Chang, P. & Gan, W. B. Development of long-term dendritic spine stability in diverse regions of cerebral cortex. *Neuron* **46**, 181–189, https://doi.org/10.1016/j.neuron.2005.04.001 (2005).
22. Greenough, W. T. *et al.* Synaptic regulation of protein synthesis and the fragile X protein. *Proceedings of the National Academy of Sciences* **98**, 7101–7106, https://doi.org/10.1073/pnas.141145998 (2001).
23. Churchill, J. D. *et al.* A converging-methods approach to fragile X syndrome. *Developmental Psychobiology* **40**, 323–338, https://doi.org/10.1002/dev.10036 (2002).
24. Bureau, I., Shepherd, G. M. G. & Svoboda, K. Circuit and Plasticity Defects in the Developing Somatosensory Cortex of Fmr1 Knock-Out Mice. *Journal of Neuroscience* **28**, 5178–5188, https://doi.org/10.1523/JNEUROSCI.1076-08.2008, NIHMS150003 (2008).

25. Alvarez, V. A. & Sabatini, B. L. Anatomical and Physiological Plasticity of Dendritic Spines. *Annual Review of Neuroscience* **30**, 79–97, https://doi.org/10.1146/annurev.neuro.30.051606.094222 (2007).

26. Kasai, H., Fukuda, M., Watanabe, S., Hayashi-Takagi, A. & Noguchi, J. Structural dynamics of dendritic spines in memory and cognition. *Trends in Neurosciences* **33**, 121–129, https://doi.org/10.1016/j.tins.2010.01.001, arXiv:1011.1669v3 (2010).

27. Sala, C. & Segal, M. Dendritic Spines: The Locus of Structural and Functional Plasticity. *Physiological Reviews* **94**, 141–188, https://doi.org/10.1152/physrev.00012.2013 (2014).

28. Fremeau, R. T. *et al.* The Expression of Vesicular Glutamate Transporters Defines Two Classes of Excitatory Synapse. *Neuron* **31**, 247–260, https://doi.org/10.1016/S0896-6273(01)00344-0 (2001).

29. Graziano, A., Liu, X.-B., Murray, K. D. & Jones, E. G. Two Sets of Glutamatergic Afferents to the Somatosensory Thalamus and Two Thalamocortical Projections in the Mouse. *J Comp Neurol* **507**, 1258–76, https://doi.org/10.1002/cne.21592 (2008).

30. Zorio, D. A. R., Jackson, C. M., Liu, Y., Rubel, E. W. & Wang, Y. Cellular distribution of the fragile X mental retardation protein in the mouse brain. *Journal of Comparative Neurology* **525**, 818–849, https://doi.org/10.1002/cne.24100 (2017).

31. Wang, G. X., Smith, S. J. & Mourrain, P. Fmr1 KO and Fenobam Treatment Differentially Impact Distinct Synapse Populations of Mouse Neocortex. *Neuron* **84**, 1273–1286, https://doi.org/10.1016/j.neuron.2014.11.016 (2014).

32. Verkhratsky, A. & Nedergaard, M. Astroglial cradle in the life of the synapse. *Philosophical Transactions of the Royal Society B: Biological Sciences* **369**, https://doi.org/10.1098/rstb.2013.0595 (2014).

33. Molofsk, A. V. *et al.* Astrocytes and disease: A neurodevelopmental perspective. *Genes and Development* **26**, 891–907, https://doi.org/10.1101/gad.188326.112 (2012).

34. Pacey, L. K. & Doering, L. C. Developmental expression of FMRP in the astrocyte lineage: Implications for fragile X syndrome. *Glia* **55**, 1601–1609, https://doi.org/10.1002/glia.20573, arXiv:1505.00300v1 (2007).

35. Jawaid, S. *et al.* Alterations in CA1 hippocampal synapses in a mouse model of fragile X syndrome. *Glia* **66**, 789–800, https://doi.org/10.1002/glia.23284 (2018).

36. Hodges, J. L. *et al.* Astrocytic Contributions to Synaptic and Learning Abnormalities in a Mouse Model of Fragile X Syndrome. *Biological Psychiatry* **82**, 139–149, https://doi.org/10.1016/j.biopsych.2016.08.036 (2017).

37. Pan, F., Aldridge, G. M., Greenough, W. T. & Gan, W.-B. Dendritic spine instability and insensitivity to modulation by sensory experience in a mouse model of fragile X syndrome. *Proceedings of the National Academy of Sciences* **107**, 17768–17773, https://doi.org/10.1073/pnas.1012496107 (2010).

38. Gonçalves, J. T., Anstey, J. E., Golshani, P. & Portera-Cailliau, C. Circuit level defects in the developing neocortex of Fragile X mice. *Nature Neuroscience* **16**, 903–909, https://doi.org/10.1038/nn.3415, 15334406 (2013).

39. He, Cynthia, X. *et al.* Tactile Defensiveness and Impaired Adaptation of Neuronal Activity in the Fmr1 Knock-Out Mouse Model of Autism. *Journal of Neuroscience* **37**, 6475–6487, https://doi.org/10.1523/JNEUROSCI.0651-17.2017 (2017).

40. Cruz-Martin, A., Crespo, M. & Portera-Cailliau, C. Delayed stabilization of dendritic spines in fragile X mice. *Journal of Neuroscience* **30**, 7793–7803 (2010).

41. Micheva, K. D. & Smith, S. J. Array Tomography: A New Tool for Imaging the Molecular Architecture and Ultrastructure of Neural Circuits. *Neuron* **55**, 25–36, https://doi.org/10.1016/j.neuron.2007.06.014, arXiv:1011.1669v3 (2007).

42. Micheva, K. D., Busse, B., Weiler, N. C., O'Rourke, N. & Smith, S. J. Single-synapse analysis of a diverse synapse population: proteomic imaging methods and markers. *Neuron* **68**, 639–53, https://doi.org/10.1016/j.neuron.2010.09.024 (2010).

43. Simhal, A. K. *et al.* Probabilistic fluorescence-based synapse detection. *PLoS Computational Biology* **13**, e1005493, https://doi.org/10.1371/journal.pcbi.1005493, 1611.05479 (2017).

44. Simhal, A. K. *et al.* A Computational Synaptic Antibody Characterization Tool for Array Tomography. *Frontiers in Neuroanatomy* **12**, 258756, https://doi.org/10.3389/fnana.2018.00051 (2018).

45. Schindelin, J. *et al.* Fiji: an open-source platform for biological-image analysis. *Nature methods* **9**, 676–82, https://doi.org/10.1038/nmeth.2019 (2012).

46. Busse, B. & Smith, S. Automated Analysis of a Diverse Synapse Population. *PLoS Computational Biology* **9**, e1002976, https://doi.org/10.1371/journal.pcbi.1002976 (2013).

47. Kreshuk, A., Koethe, U., Pax, E., Bock, D. D. & Hamprecht, F. A. Automated detection of synapses in serial section transmission electron microscopy image stacks. *PLoS ONE* **9**, e87351, https://doi.org/10.1371/journal.pone.0087351 (2014).

48. Collman, F. *et al.* Mapping Synapses by Conjugate Light-Electron Array Tomography. *Journal of Neuroscience* **35**, 5792–5807, https://doi.org/10.1523/JNEUROSCI.4274-14.2015 (2015).

49. Bass, C., Helkkula, P., De Paola, V., Clopath, C. & Bharath, A. A. Detection of axonal synapses in 3D two-photon images. *PLoS ONE* **12**, e0183309, https://doi.org/10.1371/journal.pone.0183309 (2017).

50. Araque, A., Parpura, V., Sanzgiri, R. P. & Haydon, P. G. Tripartite synapses: glia, the unacknowledged partner. *Trends in Neurosciences* **22**, 208–215 (1999).

51. Merchán-Pérez, A. *et al.* Three-dimensional spatial distribution of synapses in the neocortex: a dual-beam electron microscopy study. *Cerebral cortex* **24**, 1579–1588 (2013).

52. van Steensel, B. *et al.* Partial colocalization of glucocorticoid and mineralocorticoid receptors in discrete compartments in nuclei of rat hippocampus neurons. *Journal of Cell Science* **792**, 787–792 (1996).

53. de Winter, J. C. F. Using the Student's t-test with extremely small sample sizes. *Practical Assessment, Research & Evalutaion* **18**, 1–12 (2013).

54. Kaneko, T. & Fujiyama, F. Complementary distribution of vesicular glutamate transporters in the central nervous system. *Neuroscience Research* **42**, 243–250, https://doi.org/10.1016/S0168-0102(02)00009-3 (2002).

55. Martinez-Hernandez, A., Bell, K. P. & Norenberg, M. D. Glutamine synthetase: Glial localization in brain. *Science* **195**, 1356–1358, https://doi.org/10.1126/science.14400 (1977).

56. Anlauf, E. & Derouiche, A. Glutamine Synthetase as an Astrocytic Marker: Its Cell Type and Vesicle Localization. *Frontiers in Endocrinology* **4**, 144, https://doi.org/10.3389/fendo.2013.00144 (2013).

57. Holtmaat, A. & Svoboda, K. Experience-dependent structural synaptic plasticity in the mammalian brain. *Nature Reviews Neuroscience* **10**, 647 (2009).

58. DeFelipe, J., Alonso-Nanclares, L. & Arellano, J. I. Microstructure of the neocortex: Comparative aspects. *Journal of Neurocytology* **31**, 299–316, https://doi.org/10.1023/A:1024130211265 (2002).

59. Schüz, A. & Palm, G. Density of Neurons and Synapses. *The Journal Of Comparative Neurology* **455**, 442–455, https://doi.org/10.1371/journal.pone.0092256 (1989).

60. Calì, C. *et al.* The effects of aging on neuropil structure in mouse somatosensory cortex—A 3D electron microscopy analysis of layer 1. *PLoS ONE* **13**, e0198131, https://doi.org/10.1371/journal.pone.0198131 (2018).

61. Knott, G. W., Quairiaux, C., Genoud, C. & Welker, E. Formation of dendritic spines with GABAergic synapses induced by whisker stimulation in adult mice. *Neuron* **34**, 265–273, https://doi.org/10.1016/S0896-6273(02)00663-3 (2002).

62. Koralek, K. A., Jensen, K. F. & Killackey, H. P. Evidence for two complementary patterns of thalamic input to the rat somatosensory cortex. *Brain Research* **463**, 346–351, https://doi.org/10.1016/0006-8993(88)90408-8 (1988).

63. Meyer, H. S. *et al.* Cell Type–Specific Thalamic Innervation in a Column of Rat Vibrissal Cortex. *Cerebral cortex* **20**, 2287–2303, https://doi.org/10.1093/cercor/bhq069 (2018).

64. White, E. L. Identified neurons in mouse smi cortex which are postsynaptic to thalamocortical axon terminals: A combined golgi-electron microscopic and degeneration study. *Journal of Comparative Neurology* **181**, 627–661, https://doi.org/10.1002/cne.901810310 (1978).

65. Keller, A., White, E. L. & Cipolloni, P. B. The identification of thalamocortical axon terminals in barrels of mouse Sml cortex using immunohistochemistry of anterogradely transported lectin (Phaseolus vulgaris-leucoagglutinin). *Brain research* **343**, 159–165 (1985).

66. Bopp, R., Holler-Rickauer, S., Martin, K. A. & Schuhknecht, G. F. An Ultrastructural Study of the Thalamic Input to Layer 4 of Primary Motor and Primary Somatosensory Cortex in the Mouse. *The Journal of Neuroscience* **37**, 2435–2448, https://doi.org/10.1523/JNEUROSCI.2557-16.2017 (2017).

67. Nakamura, K. *et al*. Transiently increased colocalization of vesicular glutamate transporters 1 and 2 at single axon terminals during postnatal development of mouse neocortex: a quantitative analysis with correlation coefficient. *European Journal of Neuroscience* **28**, 1032–1046, https://doi.org/10.1111/j.1460-9568.2008.06449.x (2008).

68. Reichenbach, A., Derouiche, A. & Kirchhoff, F. Morphology and dynamics of perisynaptic glia. *Brain Research Reviews* **63**, 11–25, https://doi.org/10.1016/j.brainresrev.2010.02.003 (2010).

69. Heller, J. P., Michaluk, P., Sugao, K. & Rusakov, D. A. Probing nano-organization of astroglia with multi-color super-resolution microscopy. *Journal of Neuroscience Research* **95**, 2159–2171, https://doi.org/10.1002/jnr.24026 (2017).

70. Genoud, C. *et al*. Plasticity of Astrocytic Coverage and Glutamate Transporter Expression in Adult Mouse Cortex. *PLOS Biology* **4**, 1–8, https://doi.org/10.1371/journal.pbio.0040343 (2006).

71. Jones, T. A. & Greenough, W. T. Ultrastructural Evidence for Increased Contact between Astrocytes and Synapses in Rats Reared in a Complex Environment. *Neurobiology of Learning and Memory* **65**, 48–56, https://doi.org/10.1006/nlme.1996.0005 (1996).

72. Ishii, K. *et al. In vivo* volume dynamics of dendritic spines in the neocortex of wild-type and Fmr1 KO mice. *eNeuro* **5** (2018).

73. Amitai, Y. Thalamocortical synaptic connections: efficacy, modulation, inhibition and plasticity. *Reviews in the neurosciences* **12**, 159–174 (2001).

74. Higashimori, H. *et al*. Selective Deletion of Astroglial FMRP Dysregulates Glutamate Transporter GLT1 and Contributes to Fragile X Syndrome Phenotypes *In Vivo*. *Journal of Neuroscience* **36**, 7079–7094, https://doi.org/10.1523/JNEUROSCI.1069-16.2016 (2016).

75. Juczewski, K. *et al*. Somatosensory map expansion and altered processing of tactile inputs in a mouse model of fragile X syndrome. *Neurobiology of disease* **96**, 201–215 (2016).

76. Antoine, M. W., Langberg, T., Schnepel, P. & Feldman, D. E. Increased excitation-inhibition ratio stabilizes synapse and circuit excitability in four autism mouse models. *Neuron* **101**, 648–661 (2019).

77. Rubenstein, J. L. R. & Merzenich, M. M. Model of autism: increased ratio of excitation/inhibition in key neural systems. *Genes, Brain and Behavior* **2**, 255–267 (2003).

78. O'Donnell, C., Goncalves, J. T., Portera-Cailliau, C. & Sejnowski, T. J. Beyond excitation/inhibition imbalance in multidimensional models of neural circuit changes in brain disorders. *Elife* **6**, e26724 (2017).

79. Turko, P., Groberman, K., Browa, F., Cobb, S. & Vida, I. Differential Dependence of GABAergic and Glutamatergic Neurons on Glia for the Establishment of Synaptic Transmission. *Cerebral Cortex* (2018).

80. Risher, W. C. *et al*. Astrocytes refine cortical connectivity at dendritic spines. *Elife* **3**, e04047 (2014).

Acknowledgements

Author Contributions

A.K.S. participated in the design and analysis of the study, created the software, participated in writing of the manuscript. Y.Z. participated in the conception of the study, interpretation of data and writing of the manuscript. M.M.P. acquired the data and participated in the analysis. D.V.M. participated in the conception of the study. G.S. participated in the conception and design of the work and the writing of the manuscript. K.D.M. participated in the conception, design, analysis, interpretation and writing.

Additional Information

Supplementary information accompanies this paper at https://doi.org/10.1038/s41598-019-50240-x.

Competing Interests: K.D.M. has founder's equity interests in Aratome, LLC (Menlo Park, CA), an enterprise that produces array tomography materials and services. K.D.M. is also listed as an inventor on two US patents regarding array tomography methods that have been issued to Stanford University.

Publisher's note Springer Nature remains neutral with regard to jurisdictional claims in published maps and institutional affiliations.